ADVANCED MATERIALS INTERFACES
Open Access
www.advmatinterfaces.de

Polyelectrolyte Complexation of Chitosan and WS_2 Nanotubes

*Eimear Magee, Fengwei Xie, Stefano Farris, Andrea Dsouza, Chrystala Constantinidou, Alla Zak, Reshef Tenne, and Tony McNally**

The inclusion of tungsten disulphide nanotubes (WS_2 NTs) in chitosan, plasticized with glycerol, facilitates the formation of a polyelectrolyte complex. The glycerol interrupts the intramolecular hydrogen bonding between chitosan chains allowing positively charged protonated amines of chitosan to form a complex with negatively charged oxygen ions chemisorbed to the tungsten atoms in defects. These interactions, with the unique mechanical and chemical properties of WS_2 NTs, result in a chitosan film with superior properties relative to unfilled chitosan. Even at low WS_2 NT loadings ($\leq$1 wt%), the Young's modulus (E) increases by 59%, tensile strength (σ) by 40% and tensile toughness by 74%, compared to neat chitosan, without sacrificing ductility. Addition of highly dispersed WS_2 NTs significantly improves the gas barrier properties of chitosan, with a 50% reduction in oxygen permeability, while the addition of both glycerol and WS_2 NTs to chitosan effectively reduces the carbon dioxide permeability by 80% and the water vapor transmission rate by 90%. The intrinsic antimicrobial efficacy of chitosan against both Gram-positive and Gram-negative bacteria is enhanced on inclusion of WS_2 NTs. Polyelectrolyte complexation of WS_2 NTs and glycerol-plasticized chitosan provides a cost-effective, sustainable route to biodegradable films with desirable mechanical, gas barrier properties, and antimicrobial efficacy suitable for food packaging applications.

1. Introduction

Chitosan (C) is a polysaccharide derived from the deacetylation of chitin, which is found in the cell walls of fungi and yeasts, as well as in the exoskeleton of crustaceans. It has drawn significant attention as an alternative to petroleum derived polymers for certain applications.[1] Chitosan is of great interest due to its low cost, biodegradability, being non-toxic and it displays intrinsic antibacterial efficacy, properties required in food packaging, agriculture, pharmaceutics, biomedical treatments, cosmetics, water treatment, and textiles.[2–6] However, the application of chitosan is limited due to its relatively poor thermal stability, hydrophilicity, gas permeability, and also brittleness.[7] Therefore, there is an urgent need to improve these properties if chitosan is to compete with synthetic polymers.

Many strategies have been explored to overcome these limitations. The use

E. Magee, T. McNally
International Institute for Nanocomposites Manufacturing (IINM)
WMG
University of Warwick
Coventry CV4 7AL, UK
E-mail: t.mcnally@warwick.ac.uk

F. Xie
School of Engineering
Newcastle University
Newcastle upon Tyne NE1 7RU, UK

S. Farris
DeFENS
Department of Food
Environmental and Nutritional Science
Packaging Division
University of Milan
Via Celoria 2, Milan 20133, Italy

A. Dsouza, C. Constantinidou
Warwick Medical School
University of Warwick
Coventry CV4 7AL, UK

A. Zak
Faculty of Sciences
Holon Institute of Technology – HIT
Holon 58102, Israel

R. Tenne
Department of Molecular Chemistry and Materials Science
Weizmann Institute of Science
Rehovot 76100, Israel

The ORCID identification number(s) for the author(s) of this article can be found under https://doi.org/10.1002/admi.202300501

DOI: 10.1002/admi.202300501

of plasticizing agents is an effective method for controlling the mechanical properties and overcoming the brittleness of chitosan films.[8] Plasticizers effectively reduce the intermolecular forces between polymer chains, resulting in more flexible films due to an increase in polymer chain dynamics and resulting in adjustment of the mechanical properties.[9] Such plasticizers include ethylene glycol (EG), poly(ethylene glycol) (PEG),[10,11] oleic acid, and[12] ionic liquids.[13,14] However, glycerol (G) has proven to be a vastly popular plasticizer for biopolymers due to its non-volatility, wide availability, and hydrophilicity similar to chitosan. Moreover, glycerol can induce flexibility in chitosan films, and it is highly biocompatible.[11,15,16]

To enhance the mechanical and thermal properties of chitosan, the incorporation of nanomaterials has shown to have some advantages. Composites of chitosan with (nano)metals or (nano)metal oxides, such as iron (Fe), copper (Cu), silver (Ag), silicon (Si), zinc (Zn), zinc oxide (ZnO), titanium dioxide (TiO_2) and halloysites in the form of nanotubes, have been studied, while many enhance the antimicrobial activity of chitosan among others.[17–24] Tungsten disulphide (WS_2) nanotubes (NTs) continue to attract interest as a functional filler for biopolymers as they have a combination of beneficial properties, such as mechanical,[25–27] thermal,[28–30] optical and electrical,[31,32] including excellent solid lubrication, useful for a wide range of applications. Additionally, WS_2 NTs have been shown to be non-toxic and biocompatible.[33–35] WS_2 NTs have been studied as a functional filler when added to certain biodegradable polymers including, poly(hydroxyalkanoate)s (PHAs),[36,37] poly(ethylene succinate) (PES),[38] poly(propylene fumarate) (PPF),[39] and poly(lactic acid) (PLA),[40–45] as well as for application in vascular bioresorbable scaffolds (VBS).[46,47] WS_2 NTs have been clearly shown to readily disperse in these biopolymers as well as enhance the thermal and mechanical properties of the polymer matrix.

In this paper, we report, for the first time, to the best of our knowledge, the inclusion of WS_2 NTs in a chitosan matrix. We demonstrate that polyelectrolyte complexation of positively charged chitosan with the negatively charged surface of WS_2 NTs is a route for enhancing the properties of chitosan. To this end, the inclusion of WS_2 NTs at loadings up to 2 wt% in a blend of chitosan and glycerol (20 wt%) was investigated, and an attempt was made to understand the role polyelectrolyte complexation plays in altering the thermal, mechanical, gas barrier and antimicrobial properties of chitosan.

2. Results and Discussion

2.1. FTIR Analysis

The chemical structure of the chitosan (C) used and the molecular interactions in the blends of chitosan with glycerol (CG) alone and then with glycerol and different concentrations (0.1, 0.5, 1.0, and 2.0 wt%) of WS_2 NTs, all in film form, were examined by FTIR and shown in **Figures 1** and 2. The FTIR spectra of all composite films obtained were similar except for that for unprocessed chitosan (see Figure S1, Supporting Information). The chitosan films were prepared using acetic acid solution, which lead to the protonation of the amine groups of chitosan, dissolution and, thus, film formation,[48–50] see Figure 1). Evidence for protonation can be seen from the significant reduction in the intensity

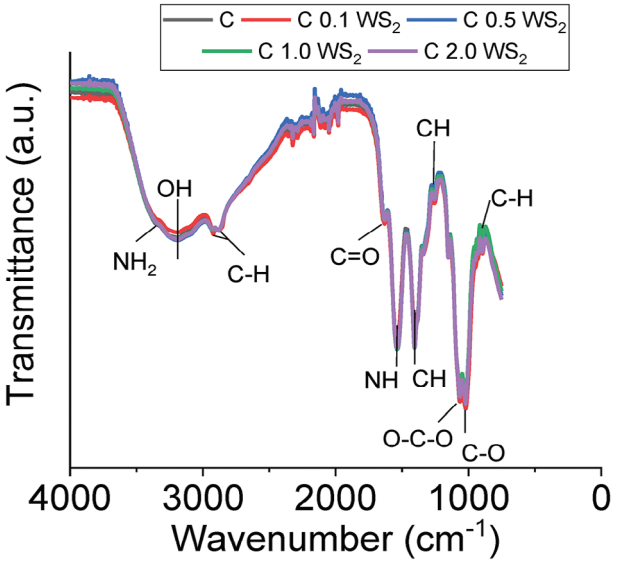

Figure 1. FTIR transmittance spectra for chitosan and composites of chitosan and WS_2 NTs with different NTs concentrations (0.1 to 2.0 wt%).

of the NH_2 peaks to form a shoulder at 3354 cm^{-1}, while there is a blueshift (13 cm^{-1}) for Amine I to 1635 cm^{-1} and for Amine III – a blueshift (63 cm^{-1}) to 1539 cm^{-1}.

Additionally, there is the emergence of new prominent peaks at 1540 cm^{-1} (C=O) and 1406 cm^{-1}, the latter derived from in-plane N—H bending and stretching (C—N and C—C) associated with Amine II.[49,51] The characteristic glycosidic linkage of chitosan, observed in the range 800 to 1200 cm^{-1}, shows no change post processing. Therefore, the processing of the chitosan films mainly involved amine groups and hydrogen bonding. WS_2 NTs are not IR-active in this range, and their FTIR spectrum (Figure S1, Supporting Information) does not display any peaks. This phenomenon is due to 1D WS_2 NTs having no dipole moment due to their symmetry which causes a change of polarizability.[52] The FTIR spectra for glycerol-plasticized chitosan (CG) films are shown in **Figure 2**, where a shift of the O—H peak by 58 to 3254 cm^{-1}, Figure 2a, in comparison to the neat chitosan film, is observed. Additionally, there is a shift of 10 cm^{-1} of the N—H bending (Amine II) peak from 1540 to 1550 cm^{-1} with the addition of glycerol, Figure 2b). The most significant changes in FTIR spectrum of CG films were seen in Figure 2c). With the addition of glycerol, the chitosan C—O—C (1063 cm^{-1}) and C—O (1021 cm^{-1}) peaks merge to form a single peak centered at 1027 cm^{-1}, suggesting strong interactions between the hydroxyl groups of chitosan and glycerol by hydrogen bonding. Additionally, there is an identifiable emergence of O—H and C—O—H peaks at 928 cm^{-1} (blue shift of 5 cm^{-1} in comparison to pure glycerol) and 850 cm^{-1}, respectively, which are attributed to glycerol peaks.

The introduction of WS_2 NTs to the CG matrix induces red shifting of the O-H and N-H (bending) peaks, Figure 2a,b) and is dependent on the loading of WS_2 NTs, see **Table 1**. The shifting obtained for CG is associated with strong intermolecular hydrogen bonding between chitosan and glycerol components but, also with a contribution associated with polyelectrolyte complexation between the positively charged amide groups of

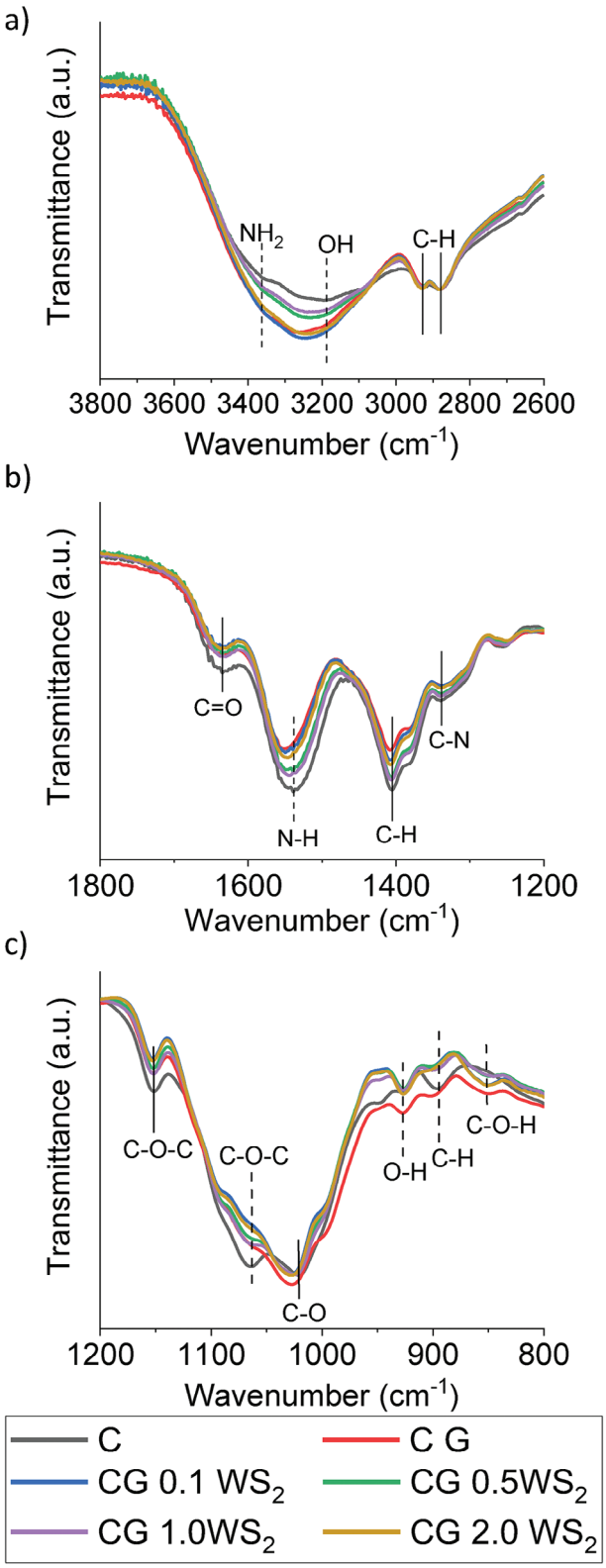

Figure 2. FTIR transmittance spectra for chitosan, chitosan:glycerol (CG) blend (80:20) and composites of this blend with up to 2 wt% WS_2 NTs in the wavenumber ranges, a) 3800–2600 cm^{-1}, b) 1800–1200 cm^{-1} and c) 1200–800 cm^{-1}.

Table 1. O—H and N—H peak positions for chitosan, CG blend (80:20) and composites of CG and WS_2 NTs.

Sample	O-H Peak position [cm^{-1}]	N-H Peak position [cm^{-1}]
C	3196	1538
CG	3254	1550
CG 0.1 wt%WS_2	3238	1546
CG 0.5 wt%WS_2	3236	1544
CG 1.0 wt%WS_2	3235	1542
CG 2.0 wt%WS_2	3244	1547

chitosan and the negatively charged oxygen species chemisorbed on the surface of the WS_2 NTs.[42] Therefore, the extent of interaction between the amine and hydroxyl moieties of chitosan with the WS_2 NTs in the CG matrix could be used as indication of the level of distribution of glycerol and the NTs in the chitosan matrix.

2.2. ATR-FTIR Mapping Analysis

To further explore polyelectrolyte complexation between chitosan and WS_2 NTs, and the distribution of the NTs and glycerol in the chitosan matrix, ATR-FTIR mapping was performed on the composites of CG and WS_2 NTs. The spectra recorded in the wavenumber range 1800–1200 cm^{-1} are shown in **Figure 3**, and in the ranges of 3500–2500, 1800–1200 (alone), and 1200–600 cm^{-1} are in Figures S2–S4 (Supporting Information). ATR-FTIR maps were produced by integrating the area under the band in the region 1535 to 1555 cm^{-1}, attributed to the N-H Amine II, (see Figure 2c) where a significant shift in peak positions was observed on blending of glycerol with, or the inclusion of WS_2 NTs in, chitosan. The area enclosed in the optical images (Figure 3-i) was mapped, and the different regions are shown as different colors (Figure 3-ii) and correlate with the variation in the intensity of area under the curve. Moreover, it should be noted that any change in intensity measured can be associated with changes in chemical composition or variation in the level of glycerol and/or WS_2 NTs dispersion in the chitosan matrix. However, both can be determined from analysis of the FTIR spectra at different points on the color contrast images. For chitosan itself, FTIR mapping (Figure 3a-iii)) shows spectra recorded for chitosan, correlating with that of previous data observed in Figure 1. However, there were individual points, red and blue intensity on the map, associated with changes in the intensity of the N—H Amide II peak at 1547 cm^{-1}. Additionally, the spectra collected from the red areas display additional peaks at 1739 cm^{-1} correlating to C=O stretching of esters, possibly from residual acetic acid in the chitosan films. From the map recorded for the CG blend (Figure 3b) significant changes in the FTIR spectrum of chitosan are observed, suggesting significant variation in chemical structure on blending with glycerol. However, the changes in color are primarily associated with the changes in the measured intensity of the N—H Amine II peak. The red and blue colors are derived from a splitting of the N—H Amine II peak, with the characteristic peak at 1546 cm^{-1} and an additional peak at 1571 cm^{-1}. The latter may be attributed to either a glycerol impurity, COO- carboxylate ions, or this peak splitting could indicate the plasticization of chitosan

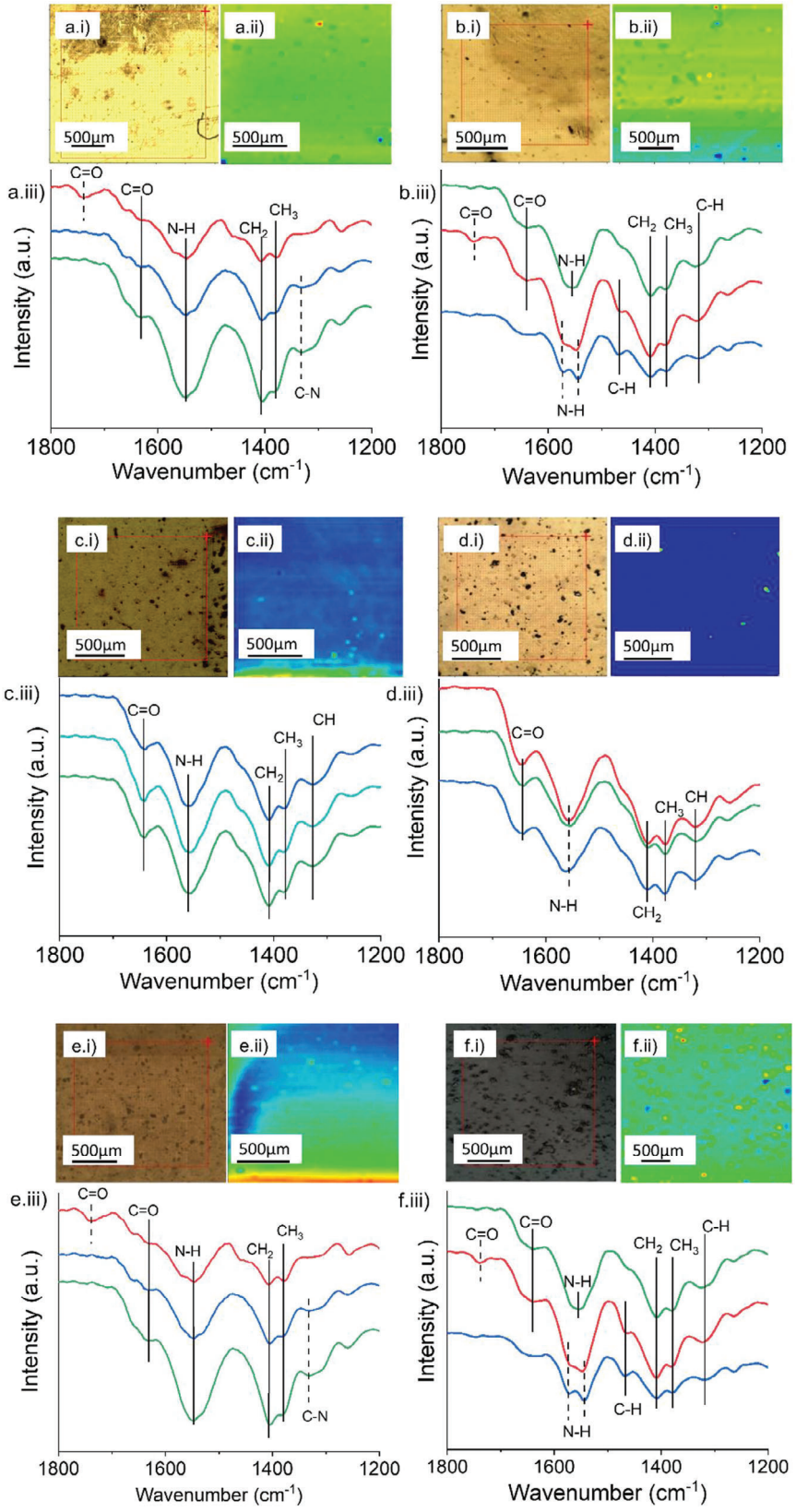

Figure 3. ATR-FTIR mapping for a) chitosan, b) CG blend (80:20) and composites of the CG blend with c) 0.1 wt%, d) 0.5 wt%, e) 1.0 wt% and f) 2.0 wt% WS_2 NTs, where i) are optical microscope images of the film surfaces, ii) is the integrated intensity of the Amide II peak and iii) are the corresponding individual pixel spectra extracted from different regions (red, blue, and green).

Table 2. Tensile mechanical properties of chitosan and composites of chitosan and C WS_2 NTs, and chitosan glycerol (CG) (80:20) blend and composites of CG and WS_2 NTs.

Sample	Young's modulus [MPa]	Maximum tensile stress [MPa]	Elongation at break [%]	Tensile toughness [J m^{-3}]
C	4273 ± 293	61 ± 3.6	15.2 ± 2.8	761 ± 67
C 0.1WS_2	3586 ± 356	56 ± 2.5	8.8 ± 1.8	454 ± 69
C 0.5WS_2	4269 ± 176	65 ± 3.5	8.5 ± 1.5	508 ± 49
C 1.0WS_2	4416 ± 274	66 ± 3.9	6.9 ± 2.5	289 ± 64
C 2.0WS_2	3714 ± 125	62 ± 4.5	7.6 ± 1.8	365 ± 72
C G	28.7 ± 0.2	17.9 ± 1.8	44.8 ± 1.3	396 ± 11
C G 0.1WS_2	45.6 ± 1.2	22.2 ± 2.9	32.4 ± 3.7	479 ± 42
C G 0.5WS_2	43.3 ± 1.1	22.5 ± 2.3	32.2 ± 2.9	473 ± 40
C G 1.0WS_2	36.4 ± 2.1	25.0 ± 7.6	46.6 ± 2.1	689 ± 67
C G 2.0WS_2	14.2 ± 0.4	9.5 ± 1.7	66.8 ± 3.5	242 ± 25

by glycerol. Previous studies[53] reported the deconvolution of Amine II peak, of which N—H bending is sensitive to hydrogen bonding. Consequently, the evolution of a peak at 1571 cm^{-1} is attributed to the hydrogen bonding of glycerol to the N—H bending (Amine II) of chitosan, causing the shift to higher wavenumbers. There is an additional peak at 1466 cm^{-1}, from the C-H stretching of CH_2 in glycerol.[54] On the inclusion of WS_2 NTs to CG, the intensity of the maps and spectra obtained during mapping were consistent, particularly for NT loadings up to 1.0 wt%, confirming uniform dispersion of the NTs in the CG matrix (Figure 3c-e). As was observed from the FTIR spectra (Figure 2), shifting of the N—H Amine II peak is identified in the spectrum of each composite. As the WS_2 NT loading in CG increases to 0.5 wt% (Figure 3d) small regions seen as red and green lines reveal a shift of the N—H peak to 1556 cm^{-1}, i.e., N—H peak from CG (Figure 3b).

However, as the WS_2 NT loading in CG was increased to 2.0 wt% (Figure 3f), there were much greater variations in the intensities and spectra obtained when mapping across the sample. Most of the spectra collected correlate with the green/blue intensities obtained and originate from similar molecular interactions between C and G but, variations in intensities are due to the distribution of the NTs in CG as WS_2 is not IR-active. The most evident change in the spectra was identified in the dark blue regions, which yield spectra similar to that of CG (Figure 3b) showing deconvolution of the Amine II peak at 1571 and 1547 cm^{-1}, spectroscopic evidence for the mechanism by which glycerol plasticize chitosan. ATR-FTIR mapping confirmed the intermolecular interaction between CG and WS_2 NTs is due to hydrogen bonding and amine ionic interactions, allowed largely by uniform dispersion and distribution of the WS_2 NTs, and glycerol in the chitosan matrix. However, when the WS_2 NTs loading was increased to 2 wt%, the less uniform distribution of the NTs and glycerol in chitosan can be seen from regions (blue/yellow) of varied molecular interaction with chitosan. Consequently, it might be expected that certain properties, including tensile mechanical properties, of composites of WS_2 NTs and chitosan, or other positively charged biopolymers, could be optimized at relatively low WS_2 NT concentrations by exploiting the favorable molecular interactions between WS_2 NTs and glycerol with chitosan. This hypothesis was tested by measuring the tensile mechanical properties of chitosan (C), CG and composites of C and CG with WS_2 NTs.

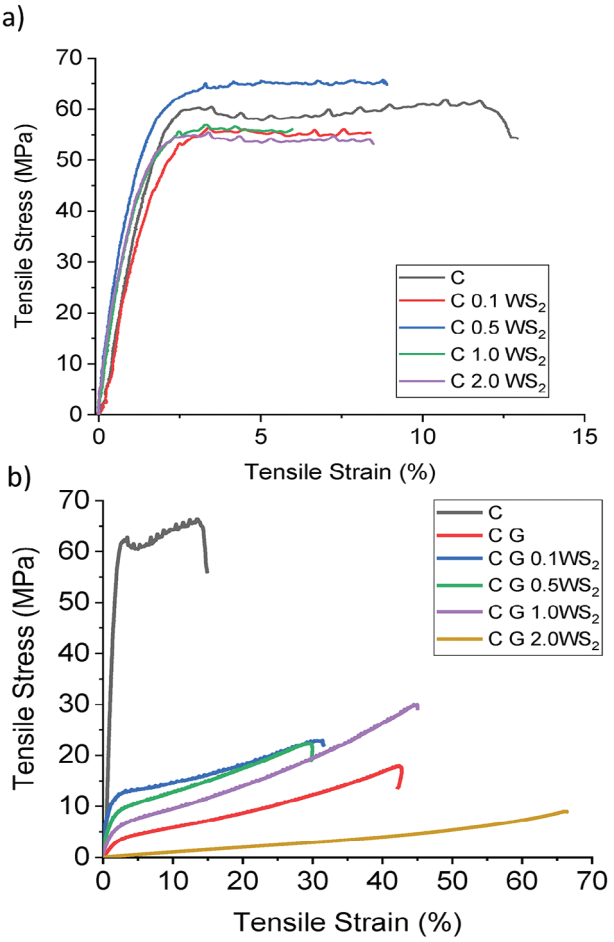

Figure 4. Representative stress-strain curves for neat chitosan films and composites of a) chitosan (C) with WS_2 NTs and b) CG with WS_2 NTs.

2.3. Tensile Mechanical Properties

The mechanical properties of chitosan and composites of chitosan with WS_2 NTs all display similar stress versus strain behavior (**Figure** 4a) as the chitosan films exhibit typical brittle behavior and weak mechanical stability[55–57]. The addition of WS_2 NTs to the neat chitosan (**Table** 2) has a minimal effect on the stiffness and strength of the chitosan film but, the elongation at break (a measure of ductility) and tensile toughness of chitosan are reduced by ≈50%. This can be attributed to the limited interfacial interaction between the surface of the NTs and chitosan alone, as seen from our ATR-FTIR mapping experiments.

The effect of inclusion of glycerol on the stress versus strain behavior of chitosan and composites of chitosan and WS_2 NTs can be clearly seen from the representative stress-strain curves shown in **Figure** 4b). As expected, the addition of glycerol to chitosan has a plasticizing effect on chitosan. Consequently, the Young's modulus and the maximum tensile stress decrease; however, a 300% increase in elongation at break is obtained. This is expected as addition of glycerol to the chitosan matrix increases the mobility of the polymer chains by decreasing the chitosan intra-polymer chain interactions.[56]

The addition of WS_2 NTs to the CG matrix results in a significant improvement in the mechanical properties of CG, Table 2. Even at low NT loadings (<0.5 wt%), the Young's modulus increased by 59%, σ increased by 40% (1 wt%), and the tensile toughness by 74% (1 wt%), in comparison to the unfilled CG films, without sacrificing ductility. This behavior is attributed to a combination of strong interfacial interaction between the NTs, glycerol and chitosan due to the NTs being homogeneously dispersed in the CG matrix. However, for a WS_2 NTs loading of 2 wt%, the plasticization effect of glycerol is highlighted by a significant decrease in the Young's modulus, maximum tensile stress as well as tensile toughness, while elongation at break of these composites increases by 50%. This result agrees with our observations from FTIR and ATR-FTIR mapping experiments, i.e., the NTs at increased loading is more difficult to disperse, and the NTs play a lesser role in competition for intermolecular interaction with CG due to NTs agglomeration. Consequently, there is more free glycerol available and the plasticization effect of glycerol on chitosan dominates. Further evidence for the extent of interaction between the composite components can be determined from the thermogravimetric analysis (TGA) of the composites in both air and nitrogen atmospheres.

2.4. Thermal Stability

Thermal Stability (TGA) conducted in an oxygen atmosphere provides additional information on the thermally induced oxidation of chitosan and composites of chitosan and WS_2 NTs with and without glycerol (**Figure** 5a,b) and Figure 5c,d), respectively. The TGA curves for glycerol and WS_2 NTs alone are given in Figure S5 (Supporting Information). Chitosan and composites of chitosan with WS_2 NTs display a similar degradation profile up to 400 °C, clearly seen from the derivative curve shown in Figure 5b. The first lower temperature process is from the evaporation of water and has a peak maximum at 95 °C, contributing to approximately an 8% mass loss from chitosan. The second stage of thermal decomposition, with a peak maximum at 260 °C, corresponds to the chemical degradation and deacetylation of chitosan, contributing to a 26% weight loss, while the addition of WS_2 NTs had a negligible impact on both these processes. The most significant difference in thermal degradation was observed above 400 °C where the decomposition temperature (T_d) of chitosan is 573 °C, and a 50% weight loss is recorded. This is associated with the oxidisation of chitosan, and of the carbonaceous residue formed during the fourth step (**Table** 3).[58,59] The addition of WS_2 NTs resulted in a slight variation of the derivative degradation peaks (±4 °C) (Figure 5b). The residue remaining above 600 °C is derived from the inorganic NTs which most probably oxidized to WO_3 at these tempertaures.

WS_2 NTs have been reported previously to oxidize beyond 400 °C.[42] TGA of the composites with glycerol shows an additional peak at 170 °C like that obtained for the TGA in a nitrogen atmosphere (Figure S6, Supporting Information), from the loss of unbound glycerol. This peak shifts to 160 °C when the WS_2 NTs are added to CG, irrespective of loading.

The peak maximum of stage 3, is associated with chemical degradation and the deacetylation of chitosan and, increases from about 260 to 272 ± 2 °C with the addition of glycerol to chitosan and composites of chitosan with WS_2 NTs. This is induced by the significant increase in hydrogen bonding in the chitosan composite network. Interestingly, the inclusion of glycerol shifts the oxidation of the composites to higher temperatures, by as much as 33°C with respect to the composites without glycerol (see Table 3). It may be that the polyelectrolyte complex formed displays intumescent behavior due to char formation, and thus a barrier to the diffusion of oxygen results in increased thermal stability[59] particularly for up to a WS_2 NT loading of 1 wt%.

2.5. XRD Analysis

It is also critical to extrapolate if changes in the properties of chitosan are due to the inclusion of the WS_2 NTs alone or from any effect the NTs having on the crystallinity of chitosan. The XRD curve of unprocessed chitosan powder (Figure S7, Supporting Information) shows peaks at $2\theta = 11.6$ ° (d-spacing = 0.76 nm) and 20.2° (d-spacing = 0.43 nm) corresponding to (020) and (110)

Table 3. Peak maxima from DTGA curves for chitosan, (CG) blend (80:20) and composites of chitosan and WS_2 NTs and, CG and WS_2 NTs.

Sample	Stage1 [°C]	Stage2 [°C]	Stage3 [°C]	Stage 4 [°C]
C	95	–	259	573
C0.1WS_2	95	–	263	585
C0.5WS_2	95	–	266	572
C1.0WS_2	95	–	257	562
C2.0WS_2	95	–	258	563
CG	69	170	273	573
CG0.1WS_2	70	160	270	596
CG0.5WS_2	70	163	271	587
CG1.0WS_2	70	160	275	595
CG2.0WS_2	70	160	273	585

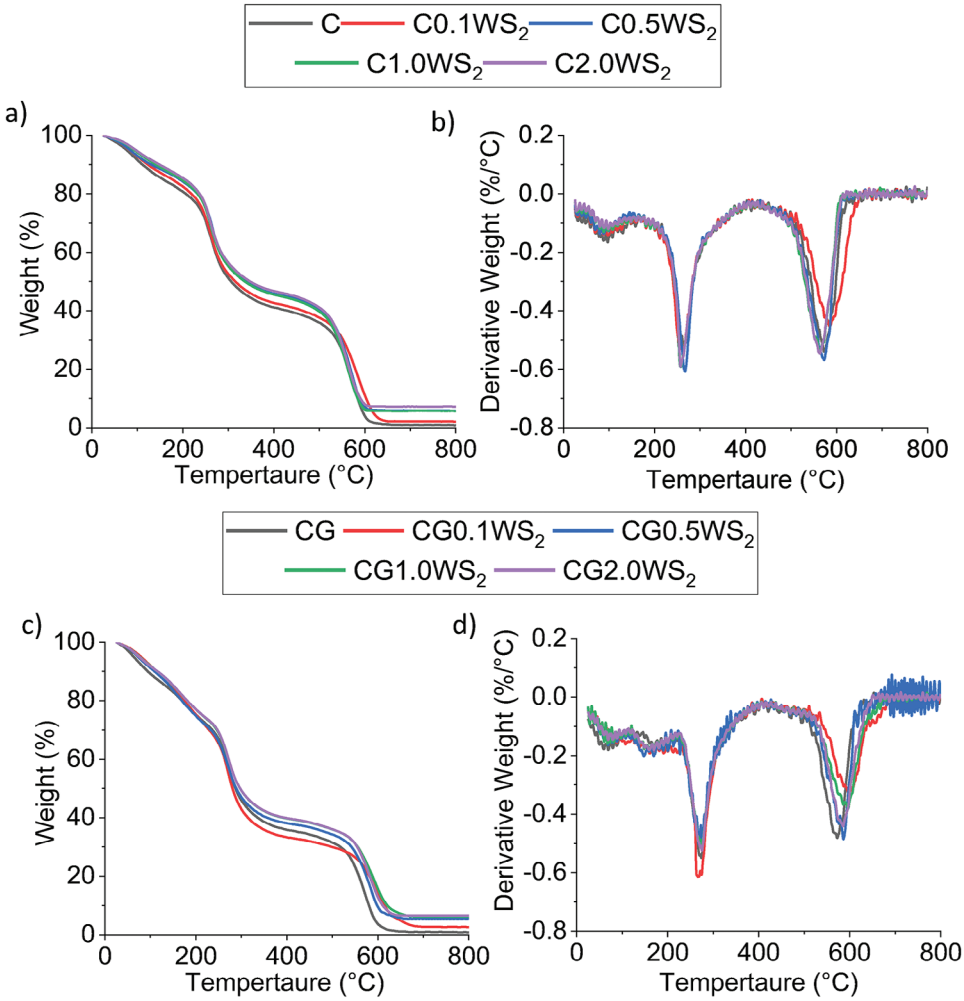

Figure 5. a) TGA and b) DTGA curves for C and composites of C and WS_2 NTs and, c) TGA and d) DTGA curves for CG and composites of CG and WS_2 NTs in air.

crystallographic planes, respectively. This data agrees with previous reports and confirms the low crystalline content of this polysaccharide.[60] XRD curves of processed chitosan and composites of chitosan and WS_2 NTs with and without glycerol are shown in **Figure 6**. All these curves display similar features however, they differ from that of unprocessed chitosan. The curve for processed chitosan shows additional peaks at $2\theta = 8.5$ and 18.3°. Additionally, a shift of the (110) peak from $2\theta = 20.2$ to 23.1° is observed, indicating a reduction in the d-spacing of the chitosan crystal lattice to 0.37 nm.

The change in the XRD pattern of processed chitosan in comparison to that of the unprocessed chitosan powder is from the processing with acetic acid almost fully destroying the original chitosan crystalline structure and, subsequently, new crystals were formed.[48,61] The impact of inclusion of the WS_2 NTs on the crystalline behavior of chitosan can be seen in Figure 6a). Characteristic peaks of WS_2 NTs can be observed at $2\theta = 14.2°$ (002), 28.7° (004) and 33.4° (101), and as expected, the intensity of these peaks increases with increasing WS_2 NT content. The addition of WS_2 NTs to chitosan also realizes the appearance of small peaks at $2\theta = 26.5°$ (101) and 27.5° (130), consistent with the α-crystalline structures of chitosan. The NTs can act as a nucleating agent and induce a small amount of crystallization of the chitosan.[62,63] Figure 6b shows the XRD curves for CG and composites of CG and WS_2 NTs. All peaks associated with the crystalline structure of chitosan are shifted to lower 2θ values when both glycerol and WS_2 NTs are added to chitosan increasing the d-spacing with increasing NT loading. Additionally, the peaks associated with chitosan become narrower and more intense, indicating a more perfect crystalline chitosan upon addition of glycerol. This, perhaps unexpected trend, indicates that, although low in content, glycerol plays a role in inducing the crystalline structure of chitosan.[64]

2.6. Raman Spectroscopy

Raman spectroscopy was also used to try and identify changes in the chemical structure of the composites through detection of the vibrational frequencies of the WS_2 NTs. **Figure 7** shows the characteristic modes for WS_2 NTs, namely E^1_{2g} and A_{1g} at 351.1 and 419.0 cm^{-1}, respectively. These are the most prominent Raman

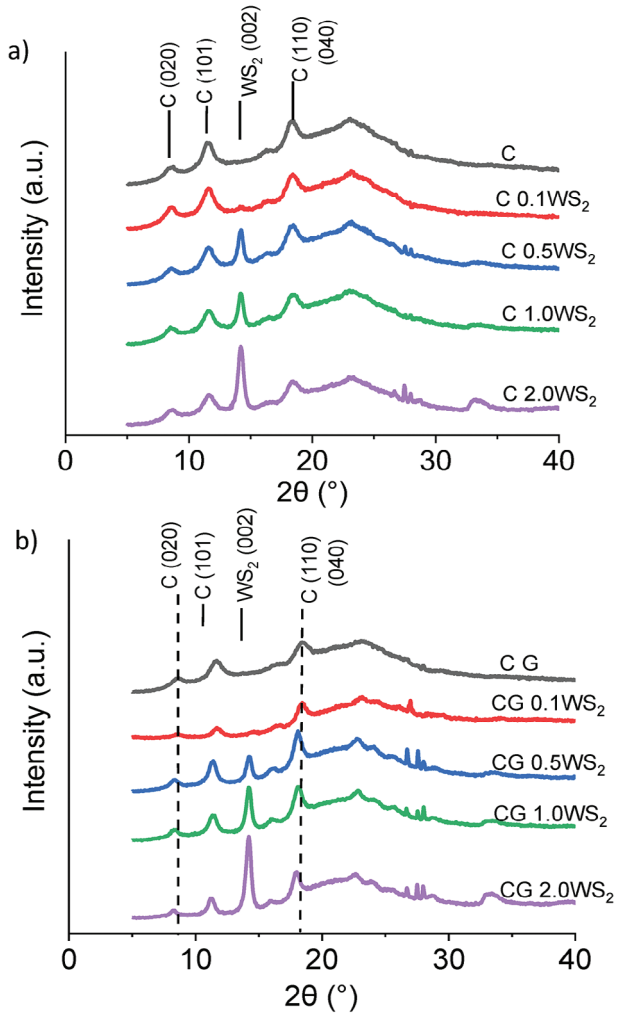

Figure 6. XRD patterns of a) composites of chitosan with WS_2 NTs and b) CG blend with WS_2 NTs.

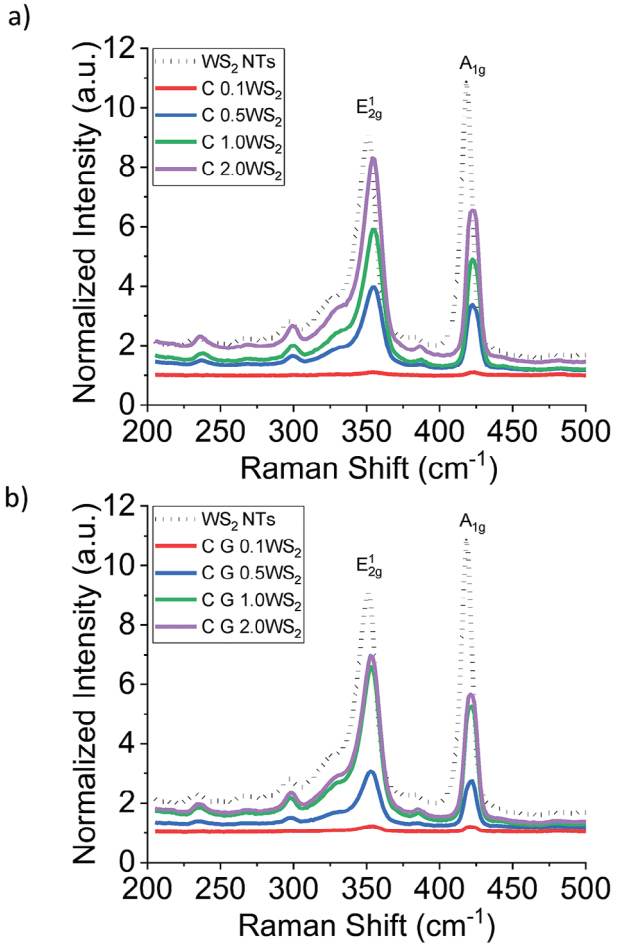

Figure 7. Raman spectra of WS_2 NTs and composites of a) chitosan, C with WS_2 NTs and b) composites of CG with WS_2 NTs showing the E^1_{2g} and A_{1g} modes.

modes of WS_2 found in the spectra (between 500 and 200 cm^{-1}) associated with the in-plane vibrations of chalcogen atoms and out-of-plane vibrations of chalcogen and transition metal atoms, respectively.[65]

The full Raman spectra (200–3000 cm^{-1}) for chitosan, glycerol, and composites of chitosan and WS_2 NTs with and without glycerol are shown in Figure S8 (Supporting Information), and the prominent peak positions for the WS_2 NTs are listed in **Table 4**. The E^1_{2g} and A_{1g} modes are indistinguishable for lower WS_2 NTs (0.1 wt%) loadings. However, the ratio of the intensity of the E^1_{2g} to A_{1g} modes (IE^1_{2g}/A_{1g}) (Table 4) increases when the NTs are added to chitosan and the CG matrix, along with a blueshift of both peak positions.

Nominally, the main Raman modes E^1_{2g} and A_{1g} are used to distinguish WS_2 structures as a function of the number of layers, and it is known that the peak positions are affected by several factors. The E^1_{2g} mode is very sensitive to uniaxial strain, while doping can change the A_{1g} mode of vibration.[66,67] In this instance, it is likely the significant changes in intensity and A_{1g} peak position is due to the surface modification of the WS_2 NTs and interaction with chitosan and glycerol.

Additionally, Deka et al.[68] suggested the $E^1{}_{2g}$ vibration is suppressed due to dispersion of NTs in confined chitosan and glycerol matrices. IE^1_{2g}/A_{1g} (Table 4) decreases for CG with 2 wt% WS_2 NTs, suggesting the WS_2 NTs are less well dispersed and interacted poorly with chitosan and glycerol, in agreement with our previous data.

2.7. Film Morphology

The application of chitosan-based films in food packaging requires a strong, flexible, and relatively tough film. All these properties can be achieved by the inclusion of WS_2 NTs to the CG matrix. The photographs in **Figure** 8a-i–iv show how brittle chitosan can be toughened and made more flexible by inclusion of glycerol and WS_2 NTs. Additionally, it is highly desirable that such films are good barriers to gases and have some degree of antibacterial efficacy. The microstructure determines the mechanical, physical and barrier properties of the film. The impact of the plasticizing effect of glycerol on

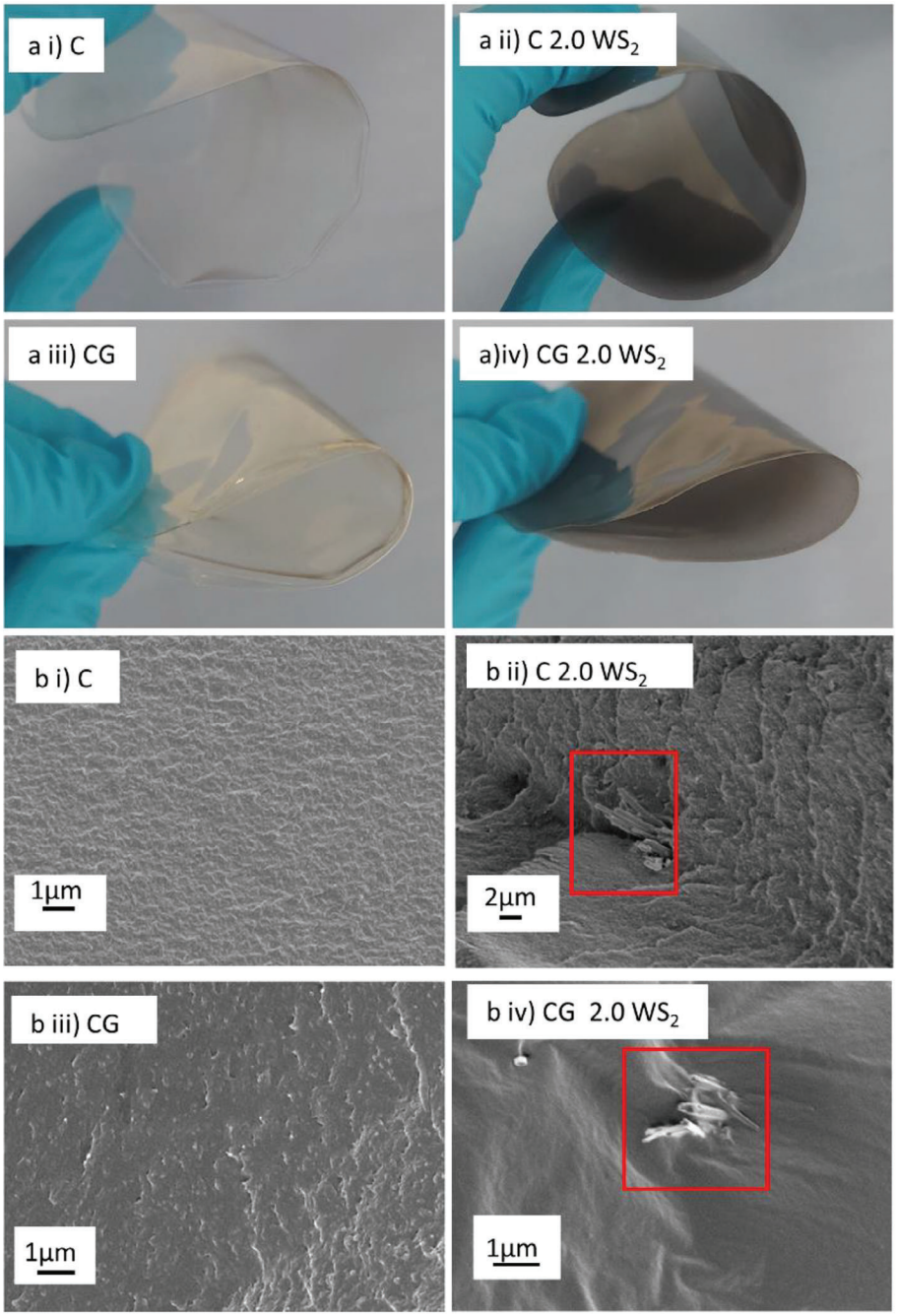

Figure 8. a-i–iv) photographs showing the increased flexibility of chitosan films containing glycerol and WS_2 NTs and b) SEM micrographs of i) chitosan, ii) composite of chitosan with WS_2 NTs, iii) CG and iv) composite of CG with 2 wt2wt% WS_2 NTs.

chitosan is clear as the chitosan film can be flexed without breaking the film. SEM was used to examine cryo-fractured cross-sections through the film thickness, Figure 8b-i–iv. SEM images of all the composites are shown in Figure S9 (Supporting Information). With a 2.0 wt% WS_2 NT loading, agglomerations of NTs can be seen, Figure 8b-iv. The addition of glycerol to chitosan (Figure 8b-iii) reveals a change in surface feature to a more cohesive texture, possibly due to the distribution of glycerol in the chitosan matrix. It may be that at 20 wt% loading, the glycerol component phase separates in chitosan to some extent.[69]

2.8. Zeta Potential Measurements

Zeta potential measurements were used to assess the surface charge of the composites as this property is known to have an impact on the antimicrobial activity of polymer films. Neat chitosan

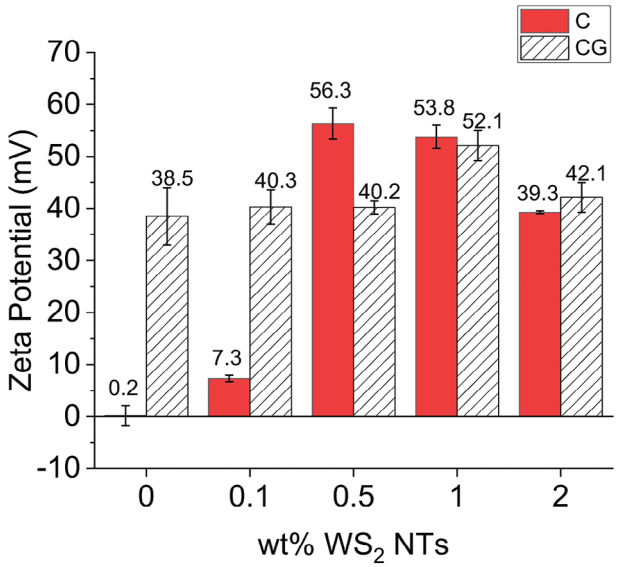

Figure 9. ζ -potential values for chitosan alone in comparison to composites of chitosan and WS_2 NTs with (CG) and without glycerol.

films, **Figure 9**, had a neutral charge which correlated with the pH value of the samples at ≈6.[70,71] The neutral charge is a consequence of the protonation of the amine functional groups in chitosan. The WS_2 NTs had a significant negative charge, a value of −26.79±0.4 mV recorded, as expected.[72] The composites of chitosan with WS_2 NTs were positively charged due to the presence of the protonated amino group ($-NH_3^+$) of chitosan. The zeta potential decreased with increasing WS_2 NTs loading up to 2 wt%, behavior attributed to less well dispersed NTs in the chitosan matrix.

The addition of glycerol, which has a positive charge of 5.26 ± 0.8 mV, to the chitosan matrix results in a significantly greater positive surface charge as the functional groups of chitosan interact with the hydroxyl group of glycerol, as reported in the FTIR data presented above. The change of surface charge of the chitosan film on inclusion of WS_2 NTs up to 1.0 wt% combined with glycerol results in a reduction in the zeta potential. This is a consequence of the insertion of glycerol (plasticizer) molecules in between the chitosan chains, resulting in partial neutralization and net zeta potential.[73] However, at higher WS_2 NTs loading, the added ions help counterbalance the effect of glycerol in reducing the zeta potential of the solution, eventually leading to an increase in the zeta potential of the solution.

Table 4. Peak positions for the E^1_{2g} and A_{1g} modes and the ratio of E^1_{2g} to A_{1g} peak intensities for WS_2 NTs and composites of WS_2 NTs with chitosan and with CG.

Sample	Wavenumber [cm^{-1}]		$IE^1_{2g}/I\,A_{1g}$
	E^1_{2g}	A_{1g}	
WS_2 NTs	350	419	0.83
C 0.1 wt% WS_2	354	423	1.00
C 0.5 wt% WS_2	355	423	1.18
C 1.0 wt% WS_2	355	423	1.20
C 2.0 wt% WS_2	355	423	1.27
C G 0.1 wt% WS_2	354	421	1.02
C G 0.5 wt% WS_2	353	422	1.11
C G 1.0 wt% WS_2	353	422	1.25
C G 2.0 wt% WS_2	353	422	1.23

Table 5. Permeability coefficient for oxygen ($P'O_2$), carbon dioxide ($P'CO_2$) and water vapour (P'WV) for chitosan, CG and composites of chitosan and WS_2 NTs with and without glycerol.

Sample	Permeability Coefficients @ 23 °C, 65% R.H.		
	$P'O_2$ [$cm^3\ m^{-2}$ 24 h^{-1} μm]	$P'CO_2$ [$cm^3\ m^{-2}$ 24 h^{-1} μm^{-1}]	P'WV [$g\ m^{-2}$ 24 h^{-1} μm^{-1}]
C	1196	1044	14291
C 0.1 wt% WS_2	481	128384	18237
C 0.5 wt% WS_2	405	126082	17405
C 1.0 wt% WS_2	573	124072	15311
C 2.0 wt% WS_2	587	160069	19593
CG	4764	2269	N.D.*
CG 0.1 wt% WS_2	N.D.*	223946	16210
CG 0.5 wt% WS_2	3007	254	N.D.*
CG 1.0 wt% WS_2	5617	921	N.D.*
CG 2.0 wt% WS_2	7266	1044	1417

N.D.* ppm of permeant (oxygen or water vapour) too high in measurement

2.9. Gas Barrier Properties

A measure of the barrier properties of these films to various gases is crucial in the evaluation of the preservation effects of products and their intended use, such as in food packaging or as a material to promote wound healing.[74] Lower oxygen and carbon dioxide permeability is beneficial for food packaging, while a moist environment gas exchange is desired. Oxygen, carbon dioxide and water vapor permeability ($P'O_2$, $P'CO_2$, and P'WV, respectively) values for chitosan and composites of chitosan and WS_2 NTs with and without glycerol are listed in **Table 5**. (The corresponding transmission rates are listed in Table S1, Supporting Information). The inclusion of WS_2 NTs results in a decrease in oxygen permeability by more than 50% for all composites, an outcome also related to the excellent dispersion of the NTs in the chitosan matrix.

However, $P'O_2$ increases with the addition of glycerol as it is a liquid and fills small voids in the composite matrix, resulting in an increase in $P'O_2$.[16,75]

Conversely, $P'CO_2$ increases significantly on addition of WS_2 NTs to chitosan, while the further addition of glycerol reverses this trend, and better barrier properties against CO_2 are obtained. For CG with the lowest WS_2 NT loading (0.5 wt%) the lowest $P'CO_2$ value of 253.8 $cm^3\ m^{-2}$ 24 h) μm is achieved, a direct outcome of the network formed due to polyelectrolyte complex formation. These results agree with previous reports where it was shown that WS_2 TMDs can contribute to highly enhanced gas adsorption properties.[76–78] The limitations of chitosan as a barrier to moisture are well documented, and the P'WV values

Table 6. Percentage decrease in bacterial viability from relative fluorescence intensity measured after 8 hours for chitosan, CG and composites of chitosan and WS_2 NTs with and without glycerol.

Sample	Decrease in viability [%]		
	S. aureus	*E. coli*	*P. fluorescens*
C	84	15	89
C 0.1 wt% WS_2	55	26	92
C 0.5 wt% WS_2	84	29	93
C 1.0 wt% WS_2	82	38	96
C 2.0 wt% WS_2	87	51	97
CG	96	29	17
C G 0.1 wt% WS_2	80	64	28
C G 0.5 wt% WS_2	55	30	31
C G 1.0 wt% WS_2	55	23	49
C G 2.0 wt% WS_2	38	13	57

obtained are typical behavior due to the hydrophilic nature of this polysaccharide. The addition of WS_2 NTs to chitosan did not yield any significant change in P'WV. However, the addition of glycerol to chitosan resulted in a significantly higher reading, to ppm level of water vapor and too high to be measured with the instrument available. However, for the composites of CG with 2.0 wt% WS_2 NTs, P'WV decreased by about 90% to that measured for the chitosan film alone. This excellent enhancement in water barrier properties is due to the interaction of the NTs with the hydrophilic –OH and –NH groups of chitosan and glycerol matrix,[79] therefore lowering the available hydrophilic groups for sorption of water vapor on the film surface.

2.10. Antimicrobial Activity

Resazurin assay was used to determine the viability of bacterial cells exposed to composites of chitosan and WS_2 NTs with and without glycerol. Viable bacteria that are metabolically active reduce resazurin, a blue-purple weak fluorescent compound (excitation: 530–570 nm) to resorufin, a pink highly fluorescent compound (emission: 580–590 nm). Unviable bacteria lack the ability to reduce resazurin, which is characterized by the absence of a color change and unaltered fluorescence intensity. Composites of chitosan and WS_2 NTs exhibited antibacterial activity against both Gram-positive and Gram-negative bacteria. For *S. aureus*, a significant reduction in bacterial viability was observed over a period of 8 h (**Figure 10**a-i) and **Table 6**). However, the introduction of WS_2 NTs alone had minimal impact on the antibacterial activity of chitosan, with an 85±2% decrease in cell viability, except for 0.1 wt% WS_2 NTs loading where the antibacterial performance was variable, as indicated by the large error bar. For uropathogenic *E. coli*, antibacterial activity increased with increasing WS_2 NTs loading in chitosan (Figure 10a-ii), Table 6). The survival rates observed suggest that composites of chitosan and WS_2 NTs are strong antibacterial agents against *P. fluorescens*, as seen by the sharp decline in bacterial viability with increased NT concentration (Figure 10a-iii). Therefore, as indicated by the percentage decrease in bacterial viability (Table 6), the NTs display varying degrees of antibacterial activity against both Gram-positive and Gram-negative bacteria. Chitosan is known to be intrinsically antibacterial due to the interaction of its cationic amino group with anionic bacterial cell walls.[80] Recent studies report the antibacterial potential of WS_2 nanoparticles due to their ability to adhere to the bacterial cell wall and compromise the organization of the cell structure.[81] Therefore, this study indicates that a combination of chitosan and WS_2 NTs into a stable composite material could potentially enhance antibacterial activity.

Furthermore, the effect of adding glycerol to the composites of chitosan and WS_2 NTs on the antimicrobial efficacy of both components was evaluated. Upon inclusion of glycerol and at lower WS_2 NT loadings, antibacterial activity against *E. coli* and *S. aureus* was obtained; however, with increasing WS_2 NT loading, an increase in bacterial viability was observed (Figure 10b-i,ii), Table 6). In comparison to the composites without glycerol, addition of glycerol reduces the level of intramolecular hydrogen bonding in chitosan altering the intrinsic antibacterial activity of chitosan and WS_2 NTs.[82] The bacterial-growth-favoring properties of CG films with increasing WS_2 NTs concentration may also be due to the ability of *E. coli* and *S. aureus* to utilize glycerol as a carbon source via dehydrogenation and/or phosphorylation pathways.[83] Since the antibacterial assay is performed in a multi-well plate, bacteria can grow both in a planktonic state and by producing biofilms. As biofilms typically form a surface barrier, bacteria may not be in direct contact with the active sites of the NTs, thereby protecting bacteria from the antibacterial activity of chitosan and/or the WS_2 NTs. However, in the absence of WS_2 NTs, CG exhibited a notable decrease in *E. coli* and *S. aureus* viability (Figure 10b-i,ii), Table 6). In contrast, CG with increasing WS_2 NTs loading decreased the viability of *P. fluorescens* (Figure 10b-iii, Table 6). As *P. fluorescens* is a non-lactose/lactic-acid fermenter, it is unable to use glycerol as a carbon source for survival, and therefore it is sensitive to the antibacterial action of chitosan and/or chitosan-WS_2 NTs. Comparative antibacterial performance of the composites of chitosan and WS_2 NTs with and without glycerol across bacteria is shown in Figure S10 (Supporting Information).

3. Conclusion

Composites of chitosan and WS_2 NTs at loadings up to 2 wt% with and without glycerol were prepared and cast in film form. The WS_2 NTs were highly dispersed and distributed in the chitosan matrix, and the addition of glycerol (as a plasticizer) further aided a more uniform NT dispersion up to a loading of 1 wt%. Strong interfacial interactions were formed between the negatively charged NTs with glycerol and chitosan via intermolecular hydrogen bonding and the positively charged amide groups of chitosan to form a polyelectrolyte complex. All three components are required to form this complex as the glycerol interrupts the intramolecular hydrogen bonding in chitosan, facilitating ionic interactions between the NTs and the protonated amines of the chitosan. The mechanical properties of the chitosan are significantly altered upon inclusion of the WS_2 NTs and complex formation. At low NT loadings (<0.5 wt%), the Young's modulus increased by 59%, σ increased by 40% (1 wt%) and the tensile toughness by 74% (1 wt%), in comparison to the unfilled CG films, without sacrificing ductility. Moreover, the incorporation of WS_2 NTs has a significant impact on the gas barrier properties of chitosan,

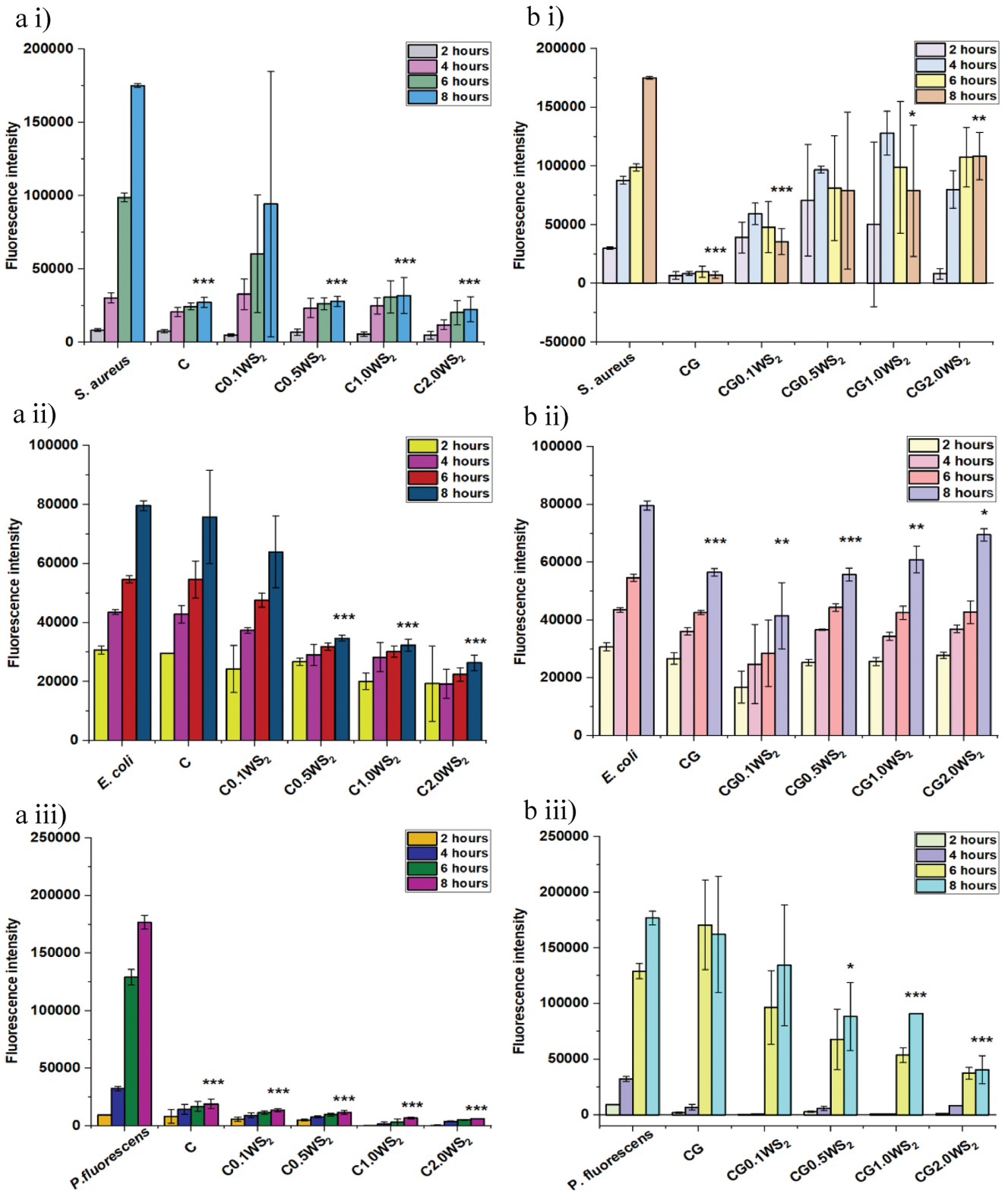

Figure 10. Antibacterial effect of composites of chitosan and WS_2 NTs a) without and b) with glycerol viability against i) *S. aureus*, ii) *E. coli*, iii) *P. fluorescens* viability over a period of 8 h. A decrease in fluorescence intensity indicates unviable bacteria for each composites calculated every 2 h in comparison with positive control – (*=p<0.05, **=p<0.01, ***=p<0.001).

with a 50% reduction in oxygen permeability, while the addition of glycerol and WS_2 NTs to chitosan effectively reduced the carbon dioxide permeability by 80% and the water vapor transmission rate by 90%, in comparison to chitosan only films. Furthermore, the intrinsic antimicrobial efficacy of CG was enhanced on inclusion of the WS_2 NTs against both Gram-positive and Gram-negative bacteria. The polyelectrolyte complexation of WS_2 NTs and glycerol-plasticized chitosan provides a cost-effective route to produce films with desirable mechanical and gas barrier properties combined with antimicrobial efficacy suitable for food packaging applications.

4. Experimental Section

Materials: WS_2 NTs were synthesized by Zak and co-workers according to the procedure published in ref. [84]. Chitosan (poly(β-(1,4)-D-glucosamine), derived from crustaceous shells, with a viscosity of about 200 mPa s and a degree of deacetylation of ≥85%, was purchased from Jinan Haidebei Marine Bioengineering Co., Ltd. (China). The molecular mass of this chitosan was about 250 kDa. Acetic acid, glacial (>95%, analytical grade) and glycerol (≥99%, analytical grade) were both purchased from Fisher Scientific UK Ltd. and used as received. Deionised water was used throughout the study.

Preparation of Chitosan-Based Composites in Film Form: A chitosan solution was prepared by dissolving 2 g of chitosan in a beaker containing 100 mL of 1% acetic acid solution. The solution was stirred at ambient temperature for 4 h until complete dissolution of the chitosan. WS_2 NTs were added to 20 mL of the prepared 1% acetic acid-water solution at four levels, 0.1, 0.5, 1.0, and 2% (w/w NTs/chitosan) and treated using ultrasound for 3 min at ambient temperature. Then the NT dispersions were added to the chitosan solutions. Glycerol-plasticized films with 0.4 g of glycerol (20% w/w of glycerol/chitosan) were added to the combined chitosan/WS_2 NTs solution. Stirring of the composite solutions was continued overnight. The solutions were then poured into Petri dishes with a 10 cm diameter, and the plates were then transferred to a fume hood under ambient conditions for 5 days. Dried films, between 200 and 300 µm thick (Table S1, Supporting Information) were peeled from the surface of the plates and stored in vacuum sealed bags in a cool and dark place prior to analysis.

Fourier Transform Infrared (FTIR) Spectroscopy: FTIR spectra of film samples were collected in transmittance mode using a Bruker Tensor 27 FTIR spectrometer. Measurements were recorded in the wavenumber range 500–4000 cm^{-1}, with a resolution of 2 cm^{-1} and 16 scans were accumulated.

Attenuated Total Reflectance – Fourier Transform Infrared (ATR-FTIR) Mapping: ATR-FTIR spectra of film samples were recorded using a Thermo Scientific – Nicolet iN 10MX instrument equipped with an attenuated total reflectance (ATR) cell with a Ge crystal at 45° and standard pressure (15 Pa). Measurements were performed in the wavenumber range 600–4000 cm^{-1} with a collection time of 5 s for 16 scans, an aperture size of 50 µm and a step size of 30 µm × 30 µm.

Mechanical (Tensile) Testing: Mechanical testing was performed using an Instron 5800R instrument with Bluehill 2 software. An average of 5–7 dog bone-shaped specimens were prepared and tested for each composite, with a crosshead speed of 1 mm min^{-1}.

Raman Spectroscopy: Raman spectra were recorded using a Horiba LabRam HR instrument (660 nm laser) under ambient conditions fitted with a 50× magnification objective and applying 25% of laser power spot focused on the sample with an exposure time of 10 s and a minimum of ten accumulations.

X-Ray Diffraction (XRD): X-ray diffraction (XRD) measurements were performed at room temperature using a third-generation Malvern Panalytical Empyrean system equipped with multicore (iCore/dCore) optics and a Pixcel3D detector operating in the 1D scanning mode. A Cu tube was used giving Cu $K_{\alpha 1/2}$ radiation (1.5419 Å). All scans were acquired in the 5 to 40° 2θ range with a step size of 0.131°.

Thermo-Gravimetric Analysis (TGA): Thermo-Gravimetric Analysis (TGA) was carried out using a Mettler Toledo thermal analyzer, in alumina pans (sample size 10–15 mg) over the temperature range of 25 to 1000 °C at a heating rate of 10 K min^{-1} in a nitrogen atmosphere.

Scanning Electron Microscopy (SEM): Micrographs were obtained using a Zeiss Sigma instrument fitted with an In Lens detector and an operating voltage of 2 kV with a magnification of 10–15k. All samples were taken from cryo-fractured specimens and sputter-coated using an Au/Pd target prior to imaging.

Zeta Potential: Zeta potential measurements were conducted on samples (1 mg mL^{-1}) in aqueous media, which were diluted with 0.5 mL methanol and vigorously shaken to ensure good dispersion before being loaded into an Omega zeta potential cuvette. Samples were run in triplicate for 100 runs at 25 °C using an Anton-Paar Litesizer 500 DLS, module type: BM10.

Gas Permeability: The barrier properties against oxygen, carbon dioxide and water vapor were assessed on a 50 cm^2 surface using a Total Perm permeability analyzer (PermTech Srl, Pieve Fosciana, Italy) equipped with both an electrochemical and an infrared sensor. Oxygen transmission rate (O_2TR), carbon dioxide transmission rate (CO_2TR) and water vapor transmission rate (WVTR) were determined according to standard methods, ASTM F1927, F2476, and F1249, respectively, with a carrier flow (N_2) of 10 mL min^{-1} at 23 °C and 65% relative humidity (RH), at one atmosphere pressure difference on the two sides of the specimen. *TR* values were then converted to permeability coefficients ($P'O_2$, $P'CO_2$, and $P'WV$) using the following Equation (1);

$$P' = P \times t = \frac{TR}{\Delta p} \times t \quad (1)$$

where, P' is the permeability coefficient [in mL µm m^{-2} (24 h^{-1}) atm^{-1} for O_2 and CO_2, in g µm m^{-2} (24h^{-1}) atm^{-1} for WVTR, P is the permeance (defined as the ratio of the *TR* to the difference between the partial pressure of the gas on the two sides of the film, Δp), and t is the total thickness of the specimen. Three replicates were run for each sample.

Antibacterial Testing: Uropathogenic *Escherichia coli* (*E. coli*) CFT073 was obtained from Dr Chrystala Constantinidou (Warwick Medical School). *Pseudomonas fluorescens* (*P. fluorescens*) and *Staphylococcus aureus* (*S. aureus*) *USA 300 JE2* were obtained from Dr Meera Unnikrishnan (Warwick Medical School). Luria-Bertani (LB) broth, Tryptic Soya Broth (TSB), and Mueller Hinton Broth – II were obtained from Merck Millipore. Bacteriological agar was obtained from Becton Dickinson & Company Difco. Resazurin sodium salt was obtained from Acros Organics.

The antibacterial performance of composites of chitosan and WS_2 NTs with and without glycerol, in film form, were evaluated against the Gram-negative bacteria uropathogenic *E. coli* CFT073 and *P. fluorescens* and the Gram-positive bacteria *S. aureus USA 300 JE2*. Bacteria were revived from glycerol stocks and streaked on Luria-Bertani (LB) agar (for *E. coli* and *P. fluorescens*) and Tryptic Soya (TSB) agar (for *S. aureus*). A single colony was picked from each plate and an overnight primary culture was set up by inoculating the colony in LB broth (for *E. coli* and *P. fluorescens*) and TS broth (for *S. aureus*). A stock solution of resazurin was prepared by dissolving 0.05 g of resazurin powder in 10 mL of 1XPBS. All experiments were carried out in sterile 24-well plates. Two milliliters of cation-adjusted Mueller Hinton Broth – II (MHB-II) was introduced in each well, followed by the addition of 10 µL stock resazurin solution to yield a final concentration of 25 µg mL^{-1}. Wells containing MHB-II and resazurin were used as negative controls. Prior to the antibacterial assay, the composites of chitosan and WS_2 NTs with and without glycerol were sterilized by exposing them to ultraviolet radiation (BIO-LINK BLX-254, 80 W) for 10 min. The UV-sterilized WS_2 NTs were introduced in negative controls to observe any bacterial growth/contamination. Absence of bacterial growth/contamination indicated successful UV-sterilization of the NTs. Wells containing MHB-II and resazurin with bacteria were used as a positive control. Test samples were introduced in the wells containing MHB-2 and resazurin. In positive controls and test wells, the overnight bacterial cultures were introduced such

that the starting optical density (OD) of bacteria at 600 nm was 0.01. The plate was incubated at 37 °C, 110 RPM for 8 h and fluorescence measurements at 585 nm were collected every 2 h over a period of 8 h using a BMG Labtech FLUOstar Omega plate reader.

Supporting Information

Supporting Information is available from the Wiley Online Library or from the author.

Acknowledgements

The authors thank WMG, University of Warwick and the Weizmann Institute of Science, Israel for funding this work via the "Weizmann UK-Making Connections" program.

Conflict of Interest

The authors declare no conflict of interest.

Data Availability Statement

The data that support the findings of this study are available from the corresponding author upon reasonable request.

Keywords

antimicrobial efficacy, barrier properties, chitosan, composite, polyelectrolyte complex, WS_2 nanotubes

Received: June 14, 2023
Revised: October 31, 2023
Published online:

[1] H. Amiri, M. Aghbashlo, M. Sharma, J. Gaffey, L. Manning, S. M. Moosavi Basri, J. F. Kennedy, V. K. Gupta, M. Tabatabaei, *Nat. Food* **2022**, *3*, 822.
[2] N. Morin-Crini, E. Lichtfouse, G. Torri, G. Crini, *Environ. Chem. Lett.* **2019**, *17*, 1667.
[3] R. Cheung, T. Ng, J. Wong, W. Chan, *Mar. Drugs* **2015**, *13*, 5156.
[4] D. Zhao, S. Yu, B. Sun, S. Gao, S. Guo, K. Zhao, *Polymers* **2018**, *10*, 462.
[5] M. Rinaudo, *Prog. Polym. Sci.* **2006**, *31*, 603.
[6] A. Muxika, A. Etxabide, J. Uranga, P. Guerrero, K. De La Caba, *Int. J. Biol. Macromol.* **2017**, *105*, 1358.
[7] I. Leceta, P. Guerrero, K. De La Caba, *Carbohydr. Polym.* **2013**, *93*, 339.
[8] W. Thakhiew, S. Devahastin, S. Soponronnarit, *J. Food Eng.* **2010**, *99*, 216.
[9] S. Ifuku, A. Ikuta, H. Izawa, M. Morimoto, H. Saimoto, *Carbohydr. Polym.* **2014**, *101*, 714.
[10] M. Shojaee Kang Sofla, S. Mortazavi, J. Seyfi, *Carbohydr. Polym.* **2020**, *232*, 115784.
[11] N. E. Suyatma, L. Tighzert, A. Copinet, V. Coma, *J. Agric. Food Chem.* **2005**, *53*, 3950.
[12] M. Vlacha, A. Giannakas, P. Katapodis, H. Stamatis, A. Ladavos, N.-M. Barkoula, *Food Hydrocolloids* **2016**, *57*, 10.
[13] P. Chen, F. Xie, F. Tang, T. McNally, *Eur. Polym. J.* **2021**, *144*, 110225.
[14] A. Sankri, A. Arhaliass, I. Dez, A. C. Gaumont, Y. Grohens, D. Lourdin, I. Pillin, A. Rolland-Sabaté, E. Leroy, *Carbohydr. Polym.* **2010**, *82*, 256.
[15] Y. Chen, Q. Duan, L. Yu, F. Xie, *Carbohydr. Polym.* **2021**, *272*, 118522.
[16] P. C. Srinivasa, M. N. Ramesh, R. N. Tharanathan, *Food Hydrocolloids* **2007**, *21*, 1113.
[17] L. Biao, S. Tan, Y. Wang, X. Guo, Y. Fu, F. Xu, Y. Zu, Z. Liu, *Mater. Sci. Eng. C* **2017**, *76*, 73.
[18] C. Chen, S. H. Lee, M. Cho, J. Kim, Y. Lee, *ACS Appl. Mater. Interfaces* **2016**, *8*, 2658.
[19] C. Ou, S. Chen, Y. Liu, J. Shao, S. Li, T. Fu, W. Fan, H. Zheng, Q. Lu, X. Bi, *J. Anal. Appl. Pyrolysis* **2016**, *122*, 268.
[20] Y. Wen, J. Ma, J. Chen, C. Shen, H. Li, W. Liu, *Chem. Eng. J.* **2015**, *259*, 372.
[21] Firnanelty, S. Chadijah, Ratna, S. Nurhuda, Sittiama, *J. Phys.: Conf. Ser.* **2021**, *1899*, 012029.
[22] S. Mallakpour, F. Sirous, C. M. Hussain, *Int. J. Biol. Macromol.* **2021**, *170*, 701.
[23] Y. Tao, J. Pan, S. Yan, B. Tang, L. Zhu, *Mater. Sci. Eng., B* **2007**, *138*, 84.
[24] G. Infurna, G. Cavallaro, G. Lazzara, S. Milioto, N. T. Dintcheva, *Polymers* **1973**, 2020, *12*,.
[25] I. Kaplan-Ashiri, S. R. Cohen, K. Gartsman, R. Rosentsveig, G. Seifert, R. Tenne, *J. Mater. Res.* **2004**, *19*, 454.
[26] I. Kaplan-Ashiri, S. R. Cohen, K. Gartsman, V. Ivanovskaya, T. Heine, G. Seifert, I. Wiesel, H. D. Wagner, R. Tenne, *Proc. Natl. Acad. Sci. USA* **2006**, *103*, 523.
[27] B. Visic, L. S. Panchakarla, R. Tenne, *J. Am. Chem. Soc.* **2017**, *139*, 12865.
[28] S. Deng, A. V. Sumant, V. Berry, *Nano Today* **2018**, *22*, 14.
[29] F. Gong, H. Duong, D. Papavassiliou, *Nanomaterials* **2016**, *6*, 142.
[30] D. Maharaj, B. Bhushan, *Mater. Lett.* **2015**, *142*, 207.
[31] G. L. Frey, R. Tenne, M. J. Matthews, M. S. Dresselhaus, G. Dresselhaus, *J. Mater. Res.* **1998**, *13*, 2412.
[32] A. Sedova, S. Khodorov, D. Ehre, B. Achrai, H. D. Wagner, R. Tenne, H. Dodiuk, S. Kenig, *J. Nanomater.* **2017**, 4838095.
[33] M. Pardo, T. Shuster-Meiseles, S. Levin-Zaidman, A. Rudich, Y. Rudich, *Environ. Sci. Technol.* **2014**, *48*, 3457.
[34] E. B. Goldman, A. Zak, R. Tenne, E. Kartvelishvily, S. Levin-Zaidman, Y. Neumann, R. Stiubea-Cohen, A. Palmon, A.-H. Hovav, D. J. Aframian, *Tissue Engineering A* **2015**, *21*, 1013.
[35] K. Ramachandran, Z. Shao, T. Di Luccio, B. Shen, E. E. Ruiz Bello, L. Tammaro, F. Villani, F. Loffredo, C. Borriello, F. Di Benedetto, E. Magee, T. McNally, J. A. Kornfield, *Acta Biomater.* **2022**, *138*, 313.
[36] T. Silverman, M. Naffakh, C. Marco, G. Ellis, *Polymers* **2018**, *10*, 166.
[37] M. Naffakh, C. Marco, G. Ellis, *CrystEngComm* **2014**, *16*, 1126.
[38] V. Asadi, S. H. Jafari, H. A. Khonakdar, L. Häußler, U. Wagenknecht, *Composites, Part B* **2016**, *98*, 496.
[39] G. Lalwani, A. M. Henslee, B. Farshid, P. Parmar, L. Lin, Y.-X. Qin, F. K. Kasper, A. G. Mikos, B. Sitharaman, *Acta Biomater.* **2013**, *9*, 8365.
[40] F. Loffredo, L. Tammaro, T. Di Luccio, C. Borriello, F. Villani, S. De Vito, K. Ramachandran, J. A. Kornfield, *Funct. Compos. Mater.* **2021**, *2*, 3.
[41] L. Tammaro, T. Di Luccio, C. Borriello, F. Loffredo, K. Ramachandran, F. Villani, F. Di Benedetto, T. Schiller, C. Minarini, J. A. Kornfield, *AIP Conf. Proc.* **2018**, *1981*, 020073.
[42] E. Magee, F. Tang, E. Ozdemir, M. Walker, T. Di Luccio, J. A. Kornfield, A. Zak, R. Tenne, T. Mcnally, *ACS Appl. Nano Mater.* **2022**, *5*, 6385.
[43] M. Naffakh, C. Marco, G. Ellis, *CrystEngComm* **2014**, *16*, 5062.
[44] M. Naffakh, C. Marco, G. Ellis, *Polymers* **2015**, *7*, 2175.
[45] M. Naffakh, C. Marco, *J. Mater. Sci.* **2015**, *50*, 6066.
[46] L. Rocher, A. S. Ylitalo, T. Di Luccio, R. Miscioscia, G. De Filippo, G. Pandolfi, F. Villani, A. Zak, G. H. Menary, A. B. Lennon, J. A. Kornfield, *Polymers* **2021**, *13*, 1764.

[47] K. Ramachandran, Z. Shao, T. Di Luccio, B. Shen, E. E. R. Bello, L. Tammaro, F. Villani, F. Loffredo, C. Borriello, F. Di Benedetto, E. Magee, T. Mcnally, J. A. Kornfield, *Acta Biomater.* **2022**, *138*, 313.
[48] P. Chen, F. Xie, F. Tang, T. McNally, *ACS Appl. Polym. Mater.* **2020**, *2*, 2957.
[49] G. Lawrie, I. Keen, B. Drew, A. Chandler-Temple, L. Rintoul, P. Fredericks, L. Grøndahl, *Biomacromolecules* **2007**, *8*, 2533.
[50] R. A. Mauricio-Sánchez, R. Salazar, J. G. Luna-Bárcenas, A. Mendoza-Galván, *Vib. Spectrosc.* **2018**, *94*, 1.
[51] Z. Chen, X. Mo, C. He, H. Wang, *Carbohydr. Polym.* **2008**, *72*, 410.
[52] Y. S. S. Leung, Novel Biopolymer Constructs: Physical Properties and Antimicrobial Efficacy, University of Warwick, **2018**.
[53] S. Rivero, L. Damonte, M. A. García, A. Pinotti, *Recent Adv. Food Sci.* **2016**, *11*, 117.
[54] M. Kachel-Jakubowska, A. Matwijczuk, M. Gagos, *Int. Agrophys.* **2017**, *31*, 175.
[55] M. I. Wahba, *J. Biomater. Sci., Polym. Ed.* **2020**, , *31*, 350.
[56] M. Cobos, B. González, M. J. Fernández, M. D. Fernández, *Int. J. Biol. Macromol.* **2018**, *114*, 599.
[57] J. Nunthanid, S. Puttipipatkhachorn, K. Yamamoto, G. E. Peck, *Drug Dev. Ind. Pharm.* **2001**, *27*, 143.
[58] M. Lavorgna, F. Piscitelli, P. Mangiacapra, G. G. Buonocore, *Carbohydr. Polym.* **2010**, *82*, 291.
[59] J. Zawadzki, H. Kaczmarek, *Carbohydr. Polym.* **2010**, *80*, 394.
[60] Y. Jampafuang, A. Tongta, Y. Waiprib, *Polymers* **2019**, *11*, 2010.
[61] S. Hajji, I. Younes, O. Ghorbel-Bellaaj, R. Hajji, M. Rinaudo, M. Nasri, K. Jellouli, *Int. J. Biol. Macromol.* **2014**, *65*, 298.
[62] O. P. Gbenebor, S. O. Adeosun, G. I. Lawal, S. Jun, S. A. Olaleye, *Eng. Sci. Technol., an International Journal* **2017**, *20*, 1155.
[63] G. Hao, Y. Hu, L. Shi, J. Chen, A. Cui, W. Weng, K. Osako, *Sci. Rep.* **2021**, *11*, 1646.
[64] E. Susilowati, I. Kartini, S. J. Santosa, Triyono, *IOP Conf. Ser.: Mater. Sci. Eng.* **2016**, *107*, 012041.
[65] A. Berkdemir, H. R. Gutiérrez, A. R. Botello-Méndez, N. Perea-López, A. L. Elías, C. I. Chia, B. Wang, V. H. Crespi, F. López-Urías, J. C. Charlier, H. Terrones, *Sci. Rep.* **2013**, *3*, 1755.
[66] A. N. Barbosa, N. S. Figueroa, M. Giarola, G. Mariotto, F. L. Freire, *Mater. Chem. Phys.* **2020**, *243*, 122599.
[67] F. Wang, I. A. Kinloch, D. Wolverson, R. Tenne, A. Zak, E. O'connell, U. Bangert, R. J. Young, *2D Mater.* **2016**, *4*, 015007.
[68] B. Deka, D. Mohanta, A. Saha, *Surf. Interfaces* **2022**, *29*, 101727.
[69] M. E. Castelló, P. S. Anbinder, J. I. Amalvy, P. J. Peruzzo, *MRS Advances* **2018**, *3*, 3601.
[70] C. Theerakarunwong, D. Boontong, *Results Chem.* **2020**, *2*, 100024.
[71] S.-H. Chang, H.-T. V. Lin, G.-J. Wu, G. J. Tsai, *Carbohydr. Polym.* **2015**, *134*, 74.
[72] E. Chibowski, A. Waksmundzki, *J. Colloid Interface Sci.* **1978**, *66*, 213.
[73] S. Prateepchanachai, W. Thakhiew, S. Devahastin, S. Soponronnarit, *Carbohydr. Polym.* **2017**, *174*, 253.
[74] H. Yilmaz Atay, *Antibacterial activity of chitosan-based systems, in Functional chitosan*, Springer, Berlin, Heidelberg **2019**, pp. 457–489.
[75] N. Akter, R. A. Khan, M. O. Tuhin, M. E. Haque, M. Nurnabi, F. Parvin, R. Islam, *J Thermoplast Compos Mater* **2012**, *27*, 933.
[76] Z. Geng, Q. Song, X. Zhang, B. Yu, Y. Shen, H. Cong, *J. Membr. Sci.* **2018**, *565*, 226.
[77] J.-H. Cha, S.-J. Choi, S. Yu, I.-D. Kim, *J. Mater. Chem. A* **2017**, *5*, 8725.
[78] N. Hassani, M. Ghorbani-Asl, B. Radha, M. Drndic, A. V. Krasheninnikov, M. Neek-Amal, *J. Phys. Chem. C* **2021**, *125*, 25055.
[79] U. Siripatrawan, P. Kaewklin, *Food Hydrocolloids* **2018**, *84*, 125.
[80] A. A. Escárcega-Galaz, D. I. Sánchez-Machado, J. López-Cervantes, A. Sanches-Silva, T. J. Madera-Santana, P. Paseiro-Losada, *Int. J. Biol. Macromol.* **2018**, *116*, 472.
[81] X. Liu, G. Duan, W. Li, Z. Zhou, R. Zhou, *RSC Adv.* **2017**, *7*, 37873.
[82] Y. E. Agustin, K. S. Padmawijaya, *IOP Conf. Ser.: Mater. Sci. Eng.* **2017**, *223*, 012046.
[83] Y. Doi, *Appl. Microbiol. Biotechnol.* **2019**, *103*, 5079.
[84] P. Chithaiah, S. Ghosh, A. Idelevich, L. Rovinsky, T. Livneh, A. Zak, *ACS Nano* **2020**, *14*, 3004.